PROCEEDINGS REPRINT

SPIE—The International Society for Optical Engineering

Reprinted from

Grazing Incidence and Multilayer X-Ray Optical Systems

27–29 July 1997
San Diego, California

Volume 3113

Uses of continuum radiation in the AXAF calibration

J. J. Kolodziejczak[a], R. A. Austin[a], R. F. Elsner[b], S. L. O'Dell[b], M. E. Sulkanen[b],
D. A. Swartz[a], A. F. Tennant[b], M. C. Weisskopf[c], G. Zirnstein[a], and W. C. McDermott[d]

[a]USRA, Marshall Space Flight Center, ES84
Huntsville, AL   35812   USA

[b]NASA, Marshall Space Flight Center, ES84
Huntsville, AL   35812   USA

[c]NASA, Marshall Space Flight Center, ES01
Huntsville, AL   35812   USA

[d]Smithsonian Astrophysical Observatory, MS-27
60 Garden St., Cambridge, MA   02138   USA

ABSTRACT

X-ray calibration of the Advanced X-ray Astrophysics Facility (AXAF) observatory at the MSFC X-Ray Calibration Facility (XRCF) made novel use of the x-ray continuum from a conventional electron-impact source. Taking advantage of the good spectral resolution of solid-state detectors, continuum measurements proved advantageous in calibrating the effective area of AXAF's High-Resolution Mirror Assembly (HRMA) and in verifying its alignment to the XRCF's optical axis.

Keywords: x rays, calibration, x-ray sources, grazing-incidence optics, detectors.

1. INTRODUCTION

In addition to its outstanding capabilities for high-resolution imaging and spectrometric imaging and for high-resolution dispersive spectroscopy, one of the unique features of the Advanced X-ray Astrophysics Facility (AXAF) is the accuracy to which it is to be calibrated. Recently, the AXAF team completed ground calibration of the AXAF observatory,[1] at the Marshall Space Flight Center (MSFC) X-Ray Calibration Facility (XRCF). Here we discuss some of the calibration measurements which employed Solid-State Detectors (SSDs) to measure the continuum x radiation produced in a conventional electron-impact source.

First (§2), we describe the standard continuum configuration used in the continuum measurements with the SSDs. Next (§3), we discuss the use of continuum measurements in calibrating the effective area of the AXAF's x-ray optic, the High-Resolution Mirror Assembly (HRMA). Then (§4.), we recount the role which continuum measurements played in verifying the alignment of the HRMA to the XRCF optical axis.

2. CONTINUUM CONFIGURATION

A significant minority of the AXAF calibration measurements at the XRCF employed continuum x radiation, rather than traditional line emission. We discuss the rationale for this approach (§2.1) and then describe the principal components of the "standard" continuum configuration for these measurements — namely, SSD monitor and focal-plane detectors (§2.2), the AXAF High-Resolution Mirror Assembly (HRMA) and relevant ground-support equipment (§2.3), and an electron-impact source operated to minimize atomic fluorescence lines (§2.4). Note that some AXAF calibration measurements employing continuum radiation used different detector configurations and also employed AXAF's objective transmission gratings.

Other author information: (Send correspondence to S.L.O.)
J.J.K.: kolodz@ssl.msfc.nasa.gov; Voice: 205-544-5498; Fax: 205-544-7754.
R.F.E.: elsner@cosmos.msfc.nasa.gov; Voice: 205-544-7741; Fax: 205-544-7754.
S.L.O.: odell@cosmos.msfc.nasa.gov; Voice: 205-544-7708; Fax: 205-544-7754.
D.A.S.: swartz@cosmos.msfc.nasa.gov; Voice: 205-544-5500; Fax: 205-544-7754.
A.F.T.: odell@cosmos.msfc.nasa.gov; Voice: 205-544-3424; Fax: 205-544-7754.
M.C.W.: martin@cosmos.msfc.nasa.gov; Voice: 205-544-7740; Fax: 205-544-7754.

2.1. Rationale

Historically, x-ray calibrations have employed electron-impact sources to produce K or L atomic fluorescence lines, interposing transmission filters to increase the spectral purity of the x-ray beam. More recently, x-ray monochromators have served to provide tuneable, (nearly) spectrally pure x-ray beams — albeit at lower flux, owing to their inherent inefficiency. Indeed, the XRCF's X-ray Source System[2] (XSS), integrated and operated by MSFC's System Analysis and Integration Laboratory (SAIL), includes the Electron-Impact Point Source (EIPS), the Double-Crystal Monochromator (DCM), and the HIgh-Resolution Erect-Field Spectrometer (HIREFS) reflection-grating monochromator.

The traditional use of proportional counters, such as the HXDS Flow Proportional Counters (FPCs), dictates the use of spectrally pure x rays in calibration. Because the proportional counter's spectral resolving power is not high (e.g., about 2.6 $\sqrt{((1\,\text{keV})/E)}$ for the HXDS FPCs), having *a priori* knowledge of the source's spectral purity is essential for an accurate calibration. However, the relatively high spectral resolving power and low noise of modern semi-conductor detectors — SSDs and Charge-Coupled Devices (CCDs) — is sufficient to determine the source's spectral content, at least at the resolution of the detector.

2.2. Solid-State Detector (SSD)

The HRMA X-ray Detection System[3] (HXDS), designed and built by the Smithsonian Astrophysical Observatory (SAO), comprises Beam-Normalization Detectors (BNDs) for monitoring x-ray-source flux and the HRMA X-ray Detector Assembly (HXDA) for focal-plane measurements. Included in the HXDS are two identical high-purity-germanium (hpGe) Solid-State Detectors[4] (SSDs): One ("SSD_5") is a (monitor) BND residing approximately 38 m from the x-ray source; the other ("SSD_X"), a (focal-plane) HXDA detector, approximately 538 m from the x-ray source. In front of each SSD lies an aperture wheel with circular apertures up to 5-mm diameter, for controlling count-rate pile-up in SSD_5 and for conducting encircled-energy measurements with SSD_X. For SSD_5, the aperture wheel also includes a Cm^{244}-excited Fe target, which provides an insertable calibration reference.

Figure 1 displays the quantum efficiency and spectral resolving power of the HXDS SSDs.[4] SAO and Physikalisch-Technische Bundesanstalt (PTB) calibrated[5] the SSD_5's quantum efficiency at the Berliner Elektronenspeicherring-Gesellschaft für Synchrotronstrahlung (BESSY). The displayed spectral resolution comes from analysis, by AXAF Project Science at MSFC, of SSD_5's response to its radioactive calibration source. Ultimately, the AXAF calibration analysis will include a detailed model for the SSD's response matrix, based on the SSD's calibration at BESSY.
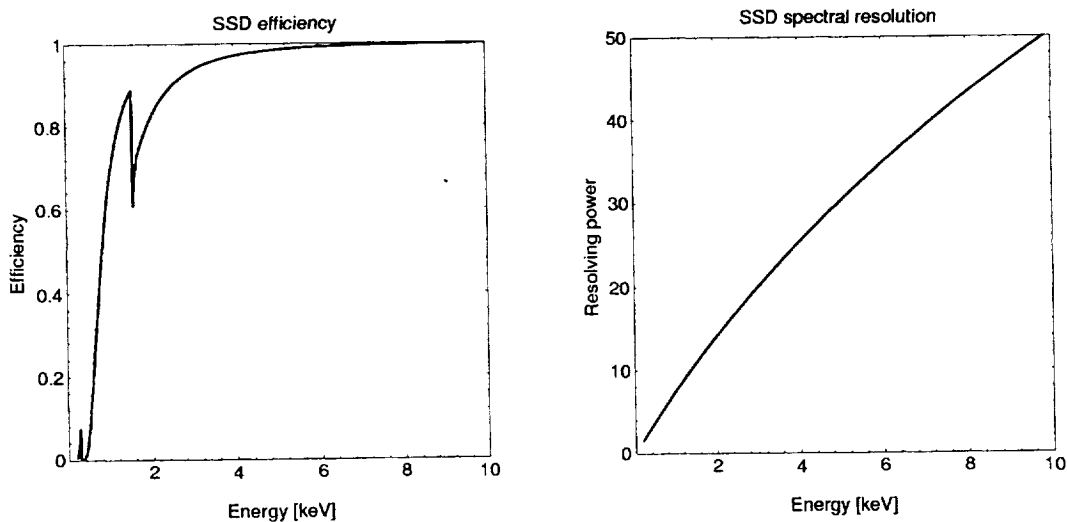

Figure 1. The high-purity germanium (hpGe) Solid-State Detector (SSD) exhibits useful quantum efficiency (> 0.1) above 0.5 keV and good spectral resolution (resolving power > 10) above 1.4 keV.

2.3. High-Resolution Mirror Assembly (HRMA)

The HRMA[6,7] has 4 nested Wolter-1 paraboloid–hyperboloid mirror shells: For historical reasons, they are identified, from the outside inward, as shells 1, 3, 4, and 6. Through much of the calibration of the AXAF observatory, a shutter system between the HRMA's exit aperture and the focal plane enabled measurements of the properties of each of the HRMA's 16 mirror-shell quadrants (Fig. 2). The Eastman Kodak Company (EKC) aligned and assembled the HRMA and provided its associated ground-support equipment, including the shutters and pitch and yaw actuators.
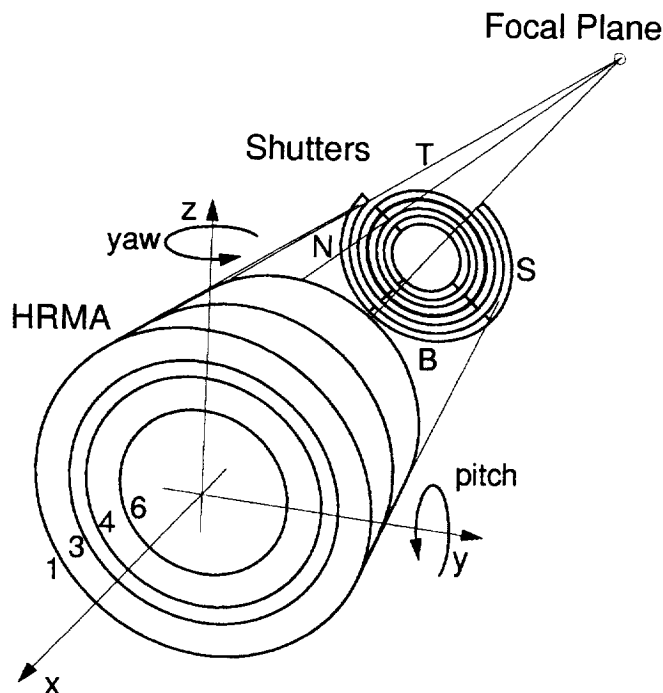

Figure 2. An assembly of 16 independent shutters isolates the converging x-ray beam of each quadrant (T=top, N=north, B=bottom, and S=south) of the HRMA's 4 mirror shells (1, 3, 4, and 6). The arrows indicate positive direction of the XRCF coordinate axes and HRMA pitch θ_y and yaw θ_z. The shutter configuration shown has the top (T) quadrant of shell 1 open and all others closed.

2.4. Electron-Impact Point Source (EIPS)

The XRCF's EIPS is a conventional electron-impact source, designed and fabricated by MSFC's System Analysis and Integration Laboratory (SAIL). With its fixed, oil-cooled anode, the EIPS can use any of a large number of conical, anode targets, to generate characteristic atomic fluorescence lines and (bremsstrahlung) continuum. The x-ray beam passes through the dual-wheel Filter-Wheel Assembly (FWA), which houses assorted, selectable transmission filters.

Traditionally, transmission filters or monochromators filter the emission of electron-impact sources, in order to enhance the spectral purity of the beam by reducing the continuum-to-line flux ratio. On the other hand, to generate x-ray continuum, without overpowering the detectors with a flux of strong lines, requires a different approach to operating the EIPS.

For most continuum measurements, we operated the EIPS with a carbon (C) target at 15 kV and inserted a beryllium (Be) filter to attenuate the lowest energies, including the C-Kα line (0.277 keV). Figure 3 shows the spectrum under these operating conditions, both for the (monitor) SSD_5 and for (focal-plane) SSD_X with only the HRMA's innermost shell unblocked by the HRMA shutters. The quotient of these 2 pulse-height-amplitude (PHA) distributions is approximately proportional to the effective area of the HRMA's innermost shell (§3).
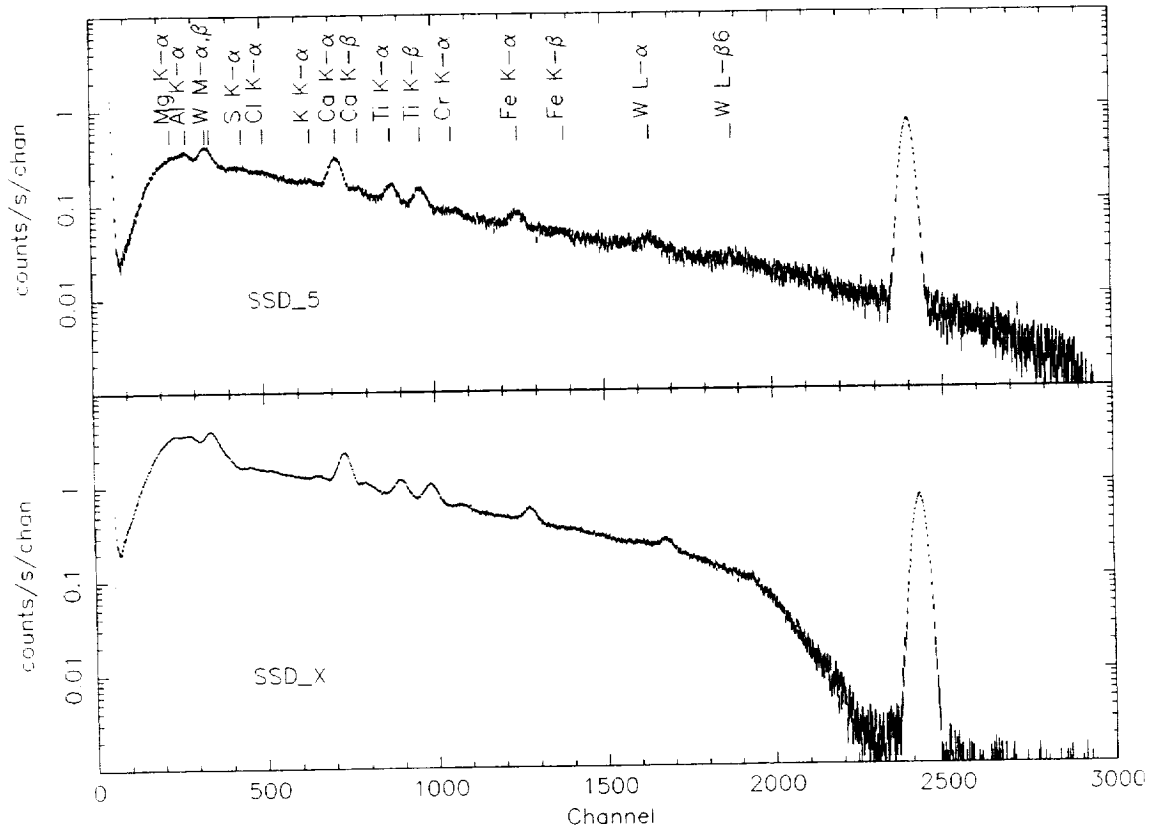
Figure 3. The SSD-measured spectrum of the EIPS with a carbon anode at 15 kV, exhibits a smooth continuum with some relatively weak, atomic fluorescence lines from contaminants in the target. The top panel is the pulse-height-amplitude (PHA) spectrum for SSD_5; the bottom, the PHA spectrum for SSD_X at the focal plane of the HRMA's innermost shell. Each PHA spectrum shows the pulser (near channel 2400); the bottom one also displays a discrete drop at the (iridium) Ir-M$_V$ edge (near channel 400) and a roll-over at the critical energy (near channel 2000) for the mirror-shell's mean grazing angle. (The energy scale is approximately 5 eV per channel.)

Beryllium (Be) may have been a better target than carbon (C) for continuum generation, because it is less porous and thus less likely to contain contaminants. On the other hand, the presence of weak lines on the continuum allowed an internal check of the SSDs' energy scale and the resolution. In addition to carbon continuum, some calibration measurements utilized a slightly different approach to generating EIPS continuum. One such approach is to operate a target (e.g., copper) at a voltage slightly below its K edge (8.98 keV for Cu) and to use a Z+1 filter (Ni-L filter for Cu-L lines) to attenuate the target's L lines.

3. EFFECTIVE-AREA CALIBRATION

One of the most important applications of continuum emission is in calibrating the absolute effective area[8] of AXAF's High-Resolution Mirror Assembly[9] (HRMA). Because there are, as yet, no celestial x-ray calibrators whose spectra are known to the desired accuracy, it is essential that the ground calibration of the effective area of the AXAF observatory be accurate and well understood. We describe the methodology for calibrating the effective area (§3.1), present the empirical result (§3.2), describe the model computation (§3.3), and compare the two (§3.4).

3.1. Methodology

In principle, the methodology for calibrating effective area is straightforward. Expose 2 identical detectors, one a beam-normalization detector and the other a focal-plane detector at the focus of the optic, to a uniform beam of radiation. At a photon energy E, the effective area $A_{eff}(E)$ of the optic's limiting aperture is approximately the following:

$$A_{eff}(E) \approx \frac{C_{fpd}(E)D_{optic}^2}{C_{bnd}(E)D_{bnd}^2}A_{bnd}. \tag{1}$$

Here, $C_{fpd}(E)$ and $C_{bnd}(E)$ are, respectively, the count rates (at energy E) in the focal-plane detector and the beam-normalization detector; D_{optic} and D_{bnd}, the distances to the optic and bnd; and A_{bnd}, the area of the bnd's aperture. Ideally, this approach does not require calibrated detectors, because the efficiencies of the *identical* detectors cancel in the count-rate ratio; only the distance ratio and the area of the beam-normalization detector's aperture must be absolutely calibrated. Of course, the accuracy of this approximation (Eq. 1) depends on the extent to which the detectors' response matrices are identical (or cross-calibrated) and upon knowledge of the beam's uniformity. Furthermore, the approximation is accurate only if (a) the radiation is spectrally pure or (b) the detector's spectral resolving power is high.

This suggests the two alternative methods for calibrating the effective area: (a) Use a monochromatic source with no constraints on the spectral resolution of the detectors; or (b) employ a continuum source with a detector having adequate spectral resolution. These 2 general methods are complementary, each having its strengths and weaknesses. The first — monochromatic source — can be accomplished with low-spectral-resolution detectors, but requires knowledge of the source's spectral purity (because a real source is not totally monochromatic) and samples only at discrete energies (thus requiring a model or interpolating scheme to fill in the spectral dependence). The second — continuous-spectrum source — simultaneously samples the entire spectrum, but only at a spectral resolution commensurate with that of the detector, and requires knowledge of the detector's response matrix (because a real detector does not have a delta-distribution response).

The ultimate calibration of the absolute effective area of the AXAF observatory will not use the simple ratio in Equation 1. Instead, parameter optimization through fitting the measured pulse-height-amplitude (PHA) spectrum with that predicted using simulations will determine the effective area. *The model is the calibration.*

3.2. Empirical determination

Here, we use Equation 1 to give a preliminary calibration of the effective area of the HRMA mirror shells, based upon measurements of continuum spectra with the HXDS's BND and focal-plane SSDs — SSD_5 and SSD_X. Figure 3 gives an example of the data used for a preliminary calibration of the effective area of HRMA shell 6 (the innermost shell). To the extent that SSD_5 and SSD_X are identical, the HRMA-shell-6 effective area at the XRCF is simply the ratio of the SSD_X pulse-height-amplitude (PHA) spectrum to that of the SSD_5, appropriately scaled for the distance ratio and BND's aperture (Eq. 1). Often the detectors' gains are not perfectly matched, so it is necessary to fine-tune the energy scale: The presence of weak lines facilitates this minor adjustment, which is made before taking the ratio of the PHA spectra.

Using the approximation of Equation 1, we determined the effective area at the XRCF of each HRMA shell (Fig. 4). For these effective-area calibration measurements, the EIPS was operated as an x-ray-continuum source, described earlier (§2.4) — namely, C target at 15 kV, with a Be transmission filter. One of the great advantages of this technique is apparent: A single measurement determines the effective area at all energies above about 1 keV, at the spectral resolution of the SSDs. Below about 1 keV, the data are unreliable, owing to the steep decline in SSD efficiency toward lower energies and to expected differences between SSD efficiencies resulting from slightly different windows and from differential accumulation of ice on the SSD windows. We note that the effective areas determined at discrete energies agree, in most cases, with those determined using the continuum measurements.

3.3. Model prediction

To predict the effective area of each HRMA shell at the XRCF, we employ the MSFC Project Science ray-trace code. This code includes the thermal pre- and post-collimators, the central aperture plate, and as-built mirror element and shell parameters (SAO/ T. Gaetz, private communication), but no figure error or surface roughness effects. Using a
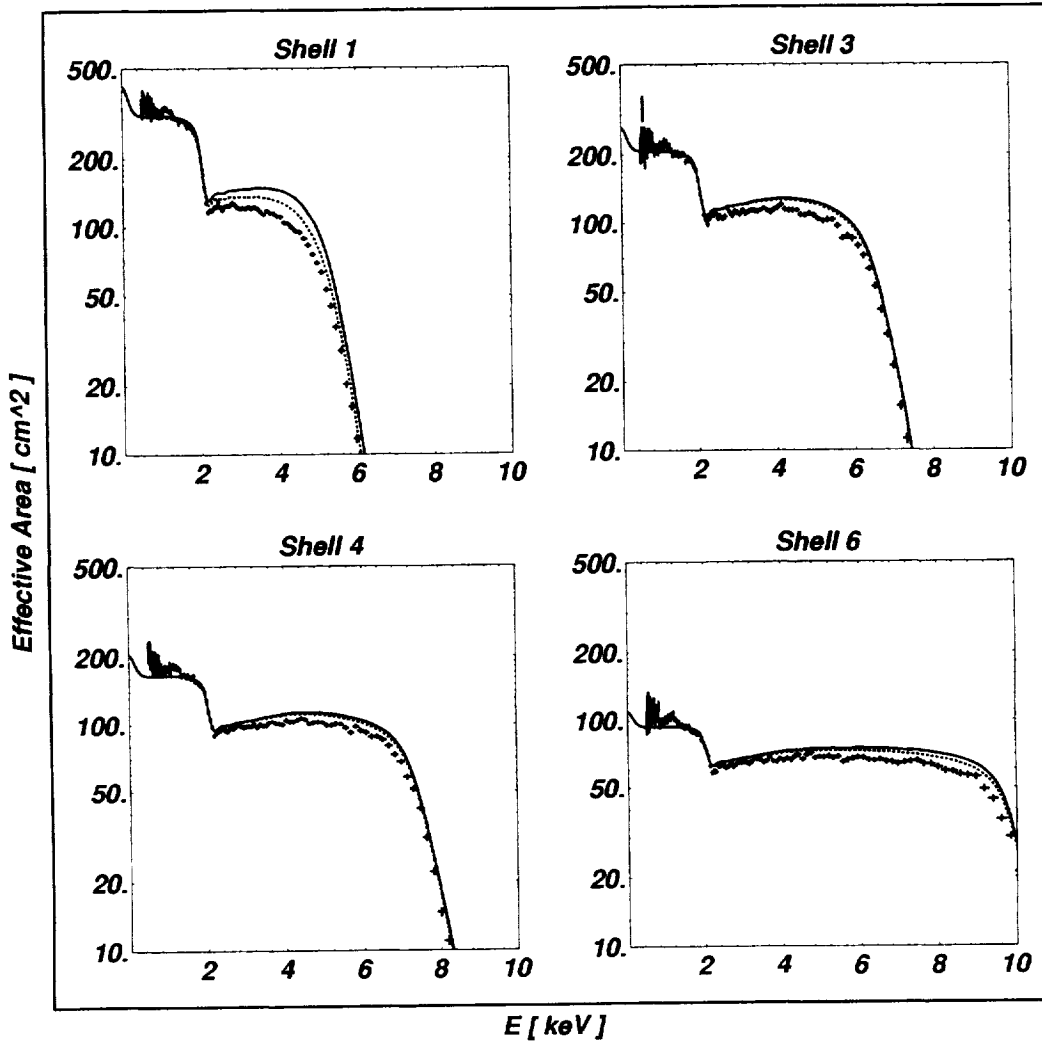
Figure 4. Comparison of measured with predicted effective area of each HRMA shell shows a discrepancy of about 10%. Data are obtained by dividing the focal-plane detector's pulse-height-amplitude (PHA) spectra by the corresponding beam-normalization detector's PHA spectrum, and scaling by the distance-ratio squared and the BND's aperture area. The solid line denotes the model prediction for the effective area over the entire focal plane; the dotted, over a 2-mm-diameter (40-arcsec) focal-plane aperture.

Monte-Carlo simulation, it records the position and direction of each ray at the nominal focal plane, as well as the grazing angle upon reflection at each mirror surface.

In post processing, a second program calculates the reflectance at each interface, for each ray stored during the Monte-Carlo simulation, using the optical constants of the mirror coating (iridium for the AXAF mirrors). Above 2 keV, we use constants[10] derived from synchrotron studies[11,12] (SAO/ D. Graessle, private communication); below 2 keV, we employ values tabulated in Ref. 13 (see http://www-cxro.lbl.gov/optical_constants). Away from edges, the synchrotron data reproduce the Henke et al.[13] data above 2 keV, when the latter are adjusted to an iridium density of 0.9725 bulk. Consequently, the reflectance computations below 2 keV assume this density for a uniform iridium coating. The MSFC code gives effective area results in agreement with those from the independent SAO ray-trace model (SAO/ D. Jerius, private communication).

In order to compare with the effective area empirically determined through continuum measurements with the SSDs (§3.2), we convolve the ray-trace-model effective areas with a gaussian of 0.21 keV FWHM, representative of the SSD's spectral resolution. Furthermore, because the focal-plane SSD measurements employed a 2-mm-diameter aperture, we decrease the predicted effective areas (over the entire focal plane) by the expected fraction of flux scattered outside the aperture. To calculate this fraction, we use the spatial power spectral densities, determined from pre-coating metrology, averaged over axial and azimuthal position for each mirror (SAO/ T. Gaetz, private communication). For shells 3, 4 and 6, this procedure gives excluded flux fractions similar to those predicted by the SAO scattering model (SAO/ D. Jerius, private communication). However, for shell 1 this procedure predicts an excluded flux fraction that rises more sharply with energy than that predicted by the SAO model.

3.4. Comparison

Even with the correction for scattering, the predicted effective areas significantly exceed the SSD measurements (Fig. 4) by about 10%. These results are preliminary: A full analysis awaits complete characterization of the SSD response and completion of the SAO synchrotron reflectivity program.[11] In addition, we are exploring the consequences of lower iridium densities,[8] finite thickness for the iridium and (binding-layer) chromium coatings (but this effect can not be important at or below the critical energy), density gradients at the surface of the iridium layer, and surface roughness. We shall also include effects due to molecular[14,15] or particulate[16,17] contamination; however, based on AXAF's very stringent contamination-control program and analyses of optical witness samples, we do not expect these effects to be significant.

4. ALIGNMENT VERIFICATION

Five ground-support actuators provide fine positioning of the HRMA in the XRCF Instrument Chamber (IC): The specified precision for controlling pitch and yaw is 10 arcsec. A laser system enables initial alignment of the HRMA Alignment Reference Mirror (ARM) to the XRCF Facility Optical Axis (FOA), to a specified 10-arcsec accuracy. Although the HRMA's effective area and point-response function are insensitive to misalignment on these scales, it is nonetheless necessary to verify the alignment in x rays. In part, this is because variations in certain HRMA parameters can affect the response in ways which are similar to off-axis effects. Without x-ray verification of the alignment, it would be more difficult to make unequivocal statements about these parameters. Here, we describe an effective x-ray alignment test (§4.1), discuss the predicted sensitivity to misalignment (§4.2), and report the results of the alignment test (§4.3).

We note that x-ray verification of the alignment proved not to be as routine as expected. Initial attempts to confirm the alignment, by comparing the line count rate through opposite shutters, failed because of an unanticipated small decenter of each HRMA hyperboloid with respect to its corresponding paraboloid. The x-ray-continuum alignment test, described below, is relatively insensitive to the decenter and enabled the unequivocal verification of the HRMA's alignment to the XRCF FOA.

4.1. Test description

The HRMA ground-support equipment included a shutter system, shown schematically in Figure 2, which can isolate any quadrants of each of HRMA's 4 mirror shells. The principal applications for the shutters was in determining best focus ("shutter focus") and in measuring paraboloid-to-hyperboloid tilt,[18] as well as in performing subaperture measurements of the point spread function (PSF).

A very sensitive test of the alignment of a grazing-incidence optic is the azimuthal dependence of the critical energy at which the response of the mirror cuts off. Using the HRMA shutters, we effectively measured the critical energy of each quadrant of each shell. To accomplish this efficiently, we employed the HXDS SSDs[4] (§2.2) to measure EIPS[2] continuum radiation (§2.4). By comparing the focal-plane SSD spectrum observed through one quadrant of a mirror shell with that of the opposite quadrant, we can determine how close the mirror shell is to being aligned in the plane of the opposing quadrants. Specifically, we divide the SSD_X Pulse-Height-Amplitude (PHA) spectrum for continuum x rays through one shell quadrant by the PHA spectrum through the opposite quadrant.

4.2. Alignment sensitivity

We constructed a simple 2-dimensional model for estimating this effect and compared it with a detailed ray-trace prediction, using the MSFC Project Science HRMA ray-trace code(3.3). The model and ray-trace calculations took into account the finite source distance (about 528 m) at the XRCF, which results in the grazing angles for the paraboloid (hyperboloid) being greater (less) than the shells' infinite-conjugate grazing angles by predicted amounts (3.6, 2.9, 2.5, and 1.9 arcmin, quadrant averaged, for shells 1, 3, 4, and 6, respectively). Both approaches predict the same sensitivity dependence, which is slightly stronger than that observed (§4.4). Owing to its shallower grazing angle, mirror shell 6 is, of course, most sensitive to misalignment. Figure 5 illustrates the predicted sensitivity to misalignment of mirror shell 6 with respect to the Facility Optical Axis (FOA): The ratio of the PHA spectra from opposite quadrants is clearly quite sensitive to misalignment, with, e.g., a 1-arcmin misalignment resulting in nearly a factor of 2 near the critical energy (9.9 keV for HRMA shell 6).
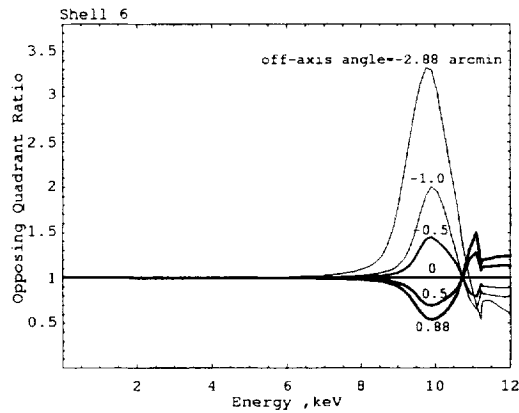

Figure 5. The ratio of quadrant throughput near the critical energy is a sensitive function of off-axis angle. This plot shows that the ratio of Pulse-Height-Amplitude (PHA) spectra for opposing quadrants of HRMA shell 6 can detect even relatively small (about 0.1 arcmin) misalignment.
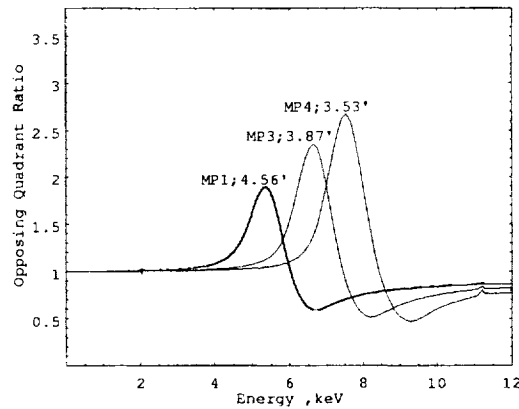

Figure 6. The sensitivity to off-axis angle, of the ratios of PHA spectra for opposing quadrants is smaller for the outer mirror shells. This plot displays expected curves for each shell's extreme off-axis measurements.

Figure 6 shows the ratio of SSD_X PHA spectra for opposing quadrants, for the other 3 HRMA shells. As the mirror-shell diameter and, hence, mean grazing angle increases, the critical energy decreases and the sensitivity becomes less. Indeed, HRMA shell 1 requires about a 4.5-times-larger off-axis angle than shell 6, to achieve a factor of 2 ratio in PHA spectra. There are two principal reasons for the decreased sensitivity for the larger diameter and, hence, larger mean-grazing-angle shells:

1. A given misalignment angle is a smaller fraction of the mean grazing angle; and

2. the grazing-angle cut off becomes less steep because the reflectance is more lossy at lower energies.

4.3. Results

X-ray alignment verification of the HRMA employed data for individual quadrants of each shell, at a number of off-axis angles. Data reduction and analysis proceeded as follows: For ease of analysis, we binned the 4096 PHA channels of the focal-plane (SSD_X) and monitor (SSD_5) detectors into blocks of 32. In order to normalize, we summed the SSD_5 PHA spectrum over the range 1.44–7.2 keV and then divided this into the SSD_X PHA spectra for each test. Next, for a given HRMA shell and off-axis angle, we divided bin-by-bin the normalized SSD_X spectrum for one quadrant by that for the opposite quadrant. Using observed atomic lines, we monitored the gain of the SSDs and found no significant gain variation.

The x-ray alignment verification probed 6 yaw and 3 pitch angles for shell 6. Figure 7 displays the test results: The tests find a PHA ratio well above 3 at the largest off-axis angle but a flat PHA ratio for the putative on-axis position. These results are in qualitative agreement with expectations. Figure 8 shows similar results for the pitch dependence. These too, are qualitatively consistent with the simple model and verify, in x rays, that the laser alignment of the HRMA ARM to the XRCF FOA was correct.
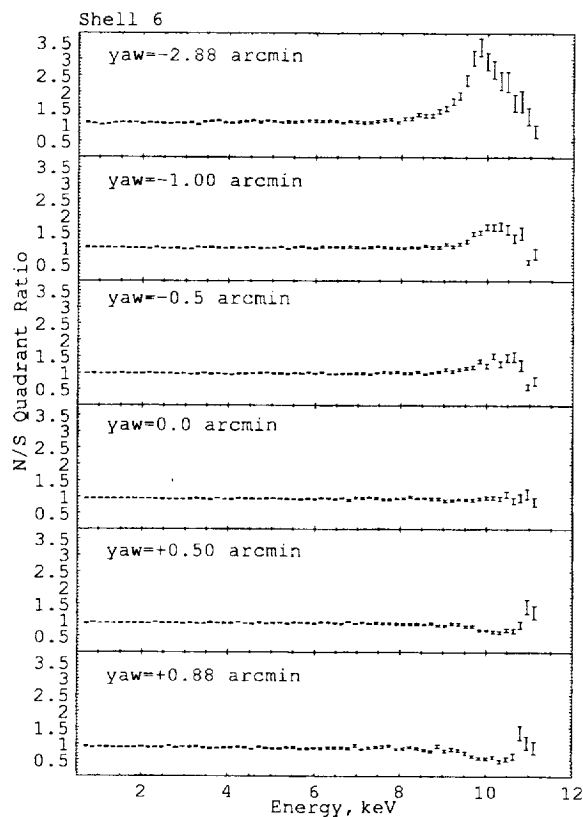

Figure 7. Ratios of normalized and binned PHA spectra for measurements made with north (N) and south (S) shell-6 shutters illustrate the sensitivity of the test to yaw. Note that the ratio is totally flat at a yaw of zero, verifying that the HRMA and FOA are aligned in yaw.

Figure 9 gives a sample of results for the remaining HRMA shells, exhibiting the results of the x-ray alignment testing at the extreme yaw for each HRMA shell. The decrease in the ratio with larger shells is again consistent with expectations (§4.2).
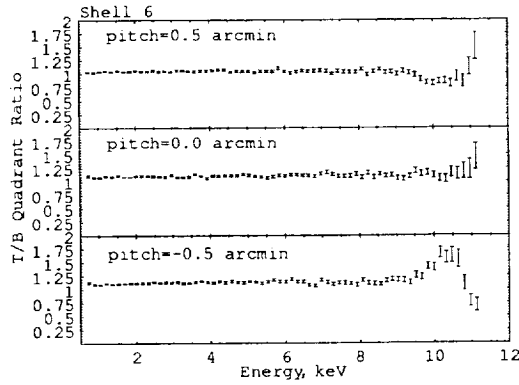
Shell 6

Figure 8. Ratios of normalized and binned PHA spectra for measurements made with top (T) and bottom (B) shell-6 shutters illustrate the sensitivity of the test to pitch. Note that the ratio is totally flat at a pitch of zero, verifying that the HRMA and FOA are aligned in pitch.
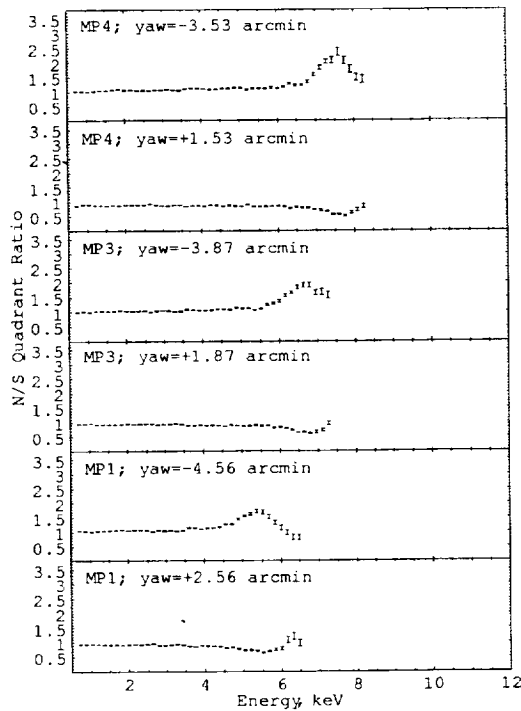

Figure 9. Ratios of normalized and binned PHA spectra for measurements made with north (N) and south (S) shutters illustrate the sensitivity of the test to yaw for HRMA shells 1, 3, and 4. This plot shows the PHA ratios at the extreme off-axis angles tested for each HRMA shell.

4.4. Conclusions

For each shell and off-axis angle, we reduced the PHA-spectrum ratio to a single value. For each shell, we selected a region of interest (ROI) for which the response is most sensitive to off-axis angle — namely, 4.8–5.92, 6.24–7.36, 7.04–8.16, and 9.28–10.4 keV, for HRMA shells 1, 3, 4, and 6, respectively. In addition, we defined a reference region of interest (ROI) corresponding to 2.4–3.52 keV. We then summed the normalized spectra over the sensitive ROI and divided by the sum over the reference ROI. Next, we divided the values for opposite quadrants to obtain a single scalar ratio for each measurement pair. Then, we performed the same manipulations for the simple model and compared

the measured with model values in a scatter plot (Fig. 10). Finally, we applied a linear fit to $R_{observed} = mR_{model} + b$, resulting in the best-fit curve shown in the Figure 10.
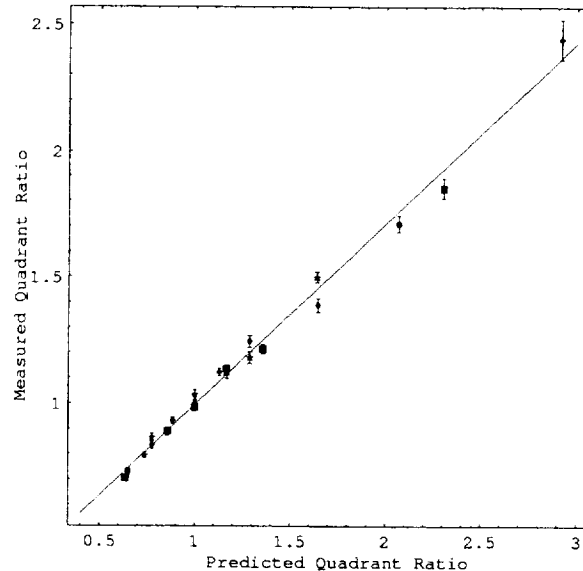

Figure 10. A comparison of measured versus fitted PHA ROI ratios, combining all measurements of pitch and of yaw, for all mirror shells, shows fair agreement with the model predictions, after scaling by about 0.7.

The best-fit parameter values and 1 sigma errors are $m = 0.713 \pm 0.014$ and $b = 0.281 \pm 0.013$. The variation in the value m from unity, and b from zero is indicative of the simplicity of the model or the analysis and, for now, prevents this method from verifying off-axis positioning accuracy.

The quantity $m + b$ is more interesting, because many sources of systematic errors cancel in the ratios. If the commanded on-axis position is really on-axis then the observed ratio should be 1 as expected, constraining $m + b$ to unity as well. The best-fit value is $m + b = 0.994$, with a 95% confidence interval ranging from 0.972 to 1.016. This corresponds to a 95% confidence interval for the on-axis facility–HRMA alignment of -2.4 to 4.1 arcsec. The implication is that the ARM, the HRMA, and the XRCF were all aligned within this angular range when on-axis.

The χ^2 for the fit was 55.0 with 25 degrees of freedom; however, we assumed no uncertainty for the commanded HRMA position. Applying the formula $\delta R = \delta\theta(dR/d\theta)$, where R is the ratio and θ is the off-axis angle, to each expected value then limits the value of $\delta\theta$. The 50% point of the cumulative χ^2 distribution for 25 degrees of freedom is $\chi^2 = 24.35$. The value of $\delta\theta$ required to obtain this χ^2 from a linear fit to the data in Figure 10 is 6 arcsec. With the worst-case assumption that errors in the commanded position are the only additional source of error, the 95% confidence interval for $\delta\theta$ ranges from 2 to 11 arcsec. This verifies that random errors in the commanded positions are within the required specifications.

In the near future, we shall apply a more realistic model to these data, in an effort to resolve the inconsistency in the best-fit values of m and b. Although the results given here show consistency between the commanded HRMA angle and the observed x-ray response, there were other periods when discrepancies between the commanded positions and laser alignment checks were reported. Quadrant data obtained during some of these times supports these reports and might be used to determine the correct alignment position. We plan to apply results of this work to such discrepant data, with the goal of resolving inconsistencies.

REFERENCES

1. M. C. Weisskopf and S. L. O'Dell, "Calibration of the AXAF observatory: Overview," in *Grazing Incidence and Multilayer X-Ray Optical Systems*, R. B. Hoover and A. B. Walker, eds., *Proc. SPIE* **3113**, 1997.

2. J. J. Kolodziejczak, R. A. Austin, R. F. Elsner, M. K. Joy, M. E. Sulkanen, E. M. Kellogg, and B. J. Wargelin, "X-ray source system at the Marshall Space Flight Center X-Ray Calibration Facility," in *X-Ray and Extreme Ultraviolet Optics*, R. B. Hoover and A. B. Walker, eds., *Proc. SPIE* **2515**, pp. 420–435, 1995.

3. B. J. Wargelin, J. P. Hughes, E. M. Kellogg, and T. J. Norton, "Ground calibration of AXAF: The HRMA X-ray Detection System," *Bull. Am. Astron. Soc.* **187**, p. 7703, 1995.

4. W. C. McDermott, E. M. Kellogg, B. J. Wargelin, I. N. Evans, S. A. Vitek, E. Y. Tsiang, D. A. Schwartz, R. Edgar, S. Kraft, F. Scholze, R. Thornagel, G. Ulm, M. Weisskopf, S. O'Dell, A. Tennant, J. Kolodziejczak, and G. Zirnstein, "The AXAF HXDS germanium solid-state-detectors," in *EUV, X-Ray, and Gamma-Ray Instrumentation for Astronomy VIII*, O. H. Siegmund and M. A. Gummin, eds., *Proc. SPIE* **3114**, 1997.

5. S. Kraft, F. Scholze, R. Thornagel, G. Ulm, W. C. McDermott, and E. M. Kellogg, "High-accuracy calibration of the HXDS hpGe detector at the PTB radiometry laboratory at BESSY," in *EUV, X-Ray, and Gamma-Ray Instrumentation for Astronomy VIII*, O. H. Siegmund and M. A. Gummin, eds., *Proc. SPIE* **3114**, 1997.

6. M. C. Weisskopf, S. L. O'Dell, R. F. Elsner, and L. P. Van Speybroeck, "Advanced X-ray Astrophysics Facility (AXAF): An overview," in *X-Ray and Extreme Ultraviolet Optics*, R. B. Hoover and A. B. Walker, eds., *Proc. SPIE* **2515**, pp. 312–329, 1995.

7. M. C. Weisskopf, S. L. O'Dell, and L. P. Van Speybroeck, "Advanced X-ray Astrophysics Facility (AXAF): An overview," in *Multilayer and Grazing Incidence X-Ray/EUV Optics III*, R. B. Hoover and A. B. Walker, eds., *Proc. SPIE* **2805**, pp. 2–7, 1996.

8. E. Kellogg, L. Cohen, R. Edgar, I. Evans, M. Freeman, T. Gaetz, D. Jerius, W. C. McDermott, P. McKinnon, S. Murray, W. Podgorski, D. Schwartz, L. Van Speybroeck, B. Wargelin, M. Zombeck, M. Weisskopf, R. Elsner, S. O'Dell, B. Ramsey, A. Tennant, J.Kolodziejczak, G. Garmire, J. Nousek, S. Kraft, F. Scholze, R. Thornagel, G. Ulm, K. Flanagan, D. Dewey, M. Bautz, S. Texter, J. Arenberg, and R. Carlson, "Absolute calibration of the AXAF telescope effective area," in *Grazing Incidence and Multilayer X-Ray Optical Systems*, R. B. Hoover and A. B. Walker, eds., *Proc. SPIE* **3113**, 1997.

9. L. P. Van Speybroeck, "HRMA performance: Expectation versus reality," in *Grazing Incidence and Multilayer X-Ray Optical Systems*, R. B. Hoover and A. B. Walker, eds., *Proc. SPIE* **3113**, 1997.

10. D. E. Graessle, A. J. Burek, J. J. Fitch, B. Harris, D. A. Schwartz, and R. L. Blake, "Optical constants from synchrotron reflectance measurements of AXAF witness mirrors 2–12 keV," in *Grazing Incidence and Multilayer X-Ray Optical Systems*, R. B. Hoover and A. B. Walker, eds., *Proc. SPIE* **3113**, 1997.

11. D. E. Graessle, J. J. Fitch, B. Harris, P. Hsieh, D. Nguyen, J. Hughes, D. A. Schwartz, and R. L. Blake, "Calibration of AXAF mirrors using synchrotron radiation," *Bull. Am. Astron. Soc.* **187**, p. 7705, 1995.

12. J. J. Fitch, A. J. Burek, A. M. Clark, D. E. Graessle, B. Harris, D. A. Schwartz, and R. L. Blake, "AXAF synchrotron witness mirror calibrations 2–12 keV," in *Grazing Incidence and Multilayer X-Ray Optical Systems*, R. B. Hoover and A. B. Walker, eds., *Proc. SPIE* **3113**, 1997.

13. B. L. Henke, E. M. Gullikson, and J. C. Davis, "X-ray interactions: Photoabsorption, scattering, transmission, and reflection at e = 50–30000 ev, z = 1–92," *Atomic Data & Nuclear Data Tables* **54**, pp. 181–342, 1993.

14. R. F. Elsner, S. L. O'Dell, and M. C. Weisskopf, "X-ray evidence for particulate contamination on the AXAF VETA-1 mirrors," in *Advances in Multilayer and Grazing Incidence X-Ray/EUV/FUV Optics*, R. B. Hoover and A. B. Walker, eds., *Proc. SPIE* **1742**, pp. 171–182, 1994.

15. D. E. Graessle, T. H. Burbine, J. J. Fitch, W. A. Podgorski, J. Z. Juda, R. F. Elsner, S. L. O'Dell, and J. M. Reynolds, "Molecular contamination study of iridium-coated x-ray mirrors," in *Advances in Multilayer and Grazing Incidence X-Ray/EUV/FUV Optics*, R. B. Hoover and A. B. Walker, eds., *Proc. SPIE* **2279**, pp. 12–26, 1994.

16. J. J. Kolodziejczak, S. L. O'Dell, R. F. Elsner, and M. C. Weisskopf, "Evidence for dust contamination on the VETA-1 mirror surface," in *Advances in Multilayer and Grazing Incidence X-Ray/EUV/FUV Optics*, R. B. Hoover and A. B. Walker, eds., *Proc. SPIE* **1742**, pp. 162–170, 1993.

17. S. L. O'Dell, R. F. Elsner, J. J. Kolodziejczak, M. C. Weisskopf, J. P. Hughes, and L. P. Van Speybroeck, "X-ray evidence for particulate contamination on the AXAF VETA-1 mirrors," in *Advances in Multilayer and Grazing Incidence X-Ray/EUV/FUV Optics*, R. B. Hoover and A. B. Walker, eds., *Proc. SPIE* **1742**, pp. 171–182, 1993.

18. T. J. Gaetz, R. J. Edgar, M. D. Freeman, W. A. Podgorski, L. P. Van Speybroeck, and P. Zhao, "Focus and alignment of the AXAF optics," in *Grazing Incidence and Multilayer X-Ray Optical Systems*, R. B. Hoover and A. B. Walker, eds., *Proc. SPIE* **3113**, 1997.